Research on the Control Strategy of Communication-Free IPT System Based on Multiparameter Joint Real-Time Identification

Lei Wang, Pan Sun, Yan Liang, Li He, Xusheng Wu, and Qijun Deng

***Abstract*—The control strategy based on parameter identification is a preferred scheme for constant-current (CC) and constant-voltage (CV) charging control of the communication-free inductive wireless transfer system, which is studied and discussed in this article. First, a multiparameter real-time identification method is introduced in detail, which is the basis of this study. Then, two control strategies based on the aforementioned identification method are proposed. One of them is the control strategy based on the PID controller and the identification results of charging information, and its working principle is described in detail. The other is a novel control strategy based on a fast calculation of the conduction angle. The conduction angle calculation process is deduced, and the working principle for CC and CV charging control is provided in detail. Experiments are carried out on a 3.6-kW prototype, and the experimental results show that both the two proposed control strategies can realize the CC and CV charging control effectively, and their response time is shorter than that of the control strategy based on wireless communication. Moreover, the control strategy based on fast calculation of conduction angle has better control performance than the PID-based control strategy because it omits the complicated design process of the controller and saves the dynamic adjusting time that the controller needs.**

***Index Terms*—Communication-free inductive wireless transfer (IPT) system, control strategy of IPT system, inductive wireless power transfer (WPT), parameter identification.**

I. Introduction

In RECENT decades, wireless power transfer (WPT) technology has undergone a rapid development. Inductive wireless power charging system (WCS), one of the WPT technologies, due to its advantages of flexibility, convenience, and no physical contact, has been widely studied in recent decades and applied to many aspects, such as biomedical devices, wireless charging of mobile phones, electrical vehicle (EV) charging, unmanned aerial vehicles (UAVs), and autonomous underwater vehicles (AUVs) [1], [2], [3], [4], [5], [6], [7], [8], [9], [10], [11].

The charging process of the battery often includes two stages, which are constant-current (CC) charging and constant-voltage (CV) charging [12]. However, the charging current and voltage of the WCS are always influenced by the change in coupling strength between coils and the variation in equivalent load resistance. Therefore, when the system parameters change, it is necessary to adopt a certain control strategy to realize the CC and CV charging control of the battery.

According to the different positions of the controller, the commonly used control strategies for CC and CV charging of the inductive wireless transfer (IPT) system can be divided into two categories, which are the secondary-side control method and the primary-side control method, respectively [12]. The secondary-side control strategy is to configure the controller on the secondary side, also called local control. By controlling the dc/dc converter at the secondary side or the active controllable rectifier, the CC and CV charging control can be realized of this kind of strategy. The advantage of the secondary-side control strategy is that it omits the wireless communication module. However, the dc/dc converter will increase the size, weight, and cost of the secondary side, and the operation of the secondary-side active rectifier requires a complicated synchronous rectifier control method and hardware circuit [13], [14], [15]. For UAVs, AUVs, and other electrical equipment with limited battery capacity, the receiving side should be as compact and lightweight as possible. Therefore, for such application scenarios, the primary-side control strategy is more suitable than the secondary-side control strategy [16], [17].

The primary-side control strategy is to configure the controller on the primary side, and its operating principle is to control the charging current or voltage by controlling the primary-side dc/dc converter or the H-bridge inverter. Therefore, the primary-side control strategy makes up for the deficiency of the secondary-side control strategy. By placing the control circuit on the primary side, the volume and weight of the secondary side can be effectively reduced. However, the primary-side control strategy usually relies on the wireless communication module to feedback charging information [18], [19], [20], [21], [22],

Manuscript received 14 June 2023; revised 17 September 2023; accepted 14 October 2023. Date of publication 30 October 2023; date of current version 6 December 2023. This work was supported in part by the National Natural Science Foundation of China under Grants 52007195 and 52207182 and in part by the National Key Research and Development Program of China under Grant 2022YFC3102800. Recommended for publication by Associate Editor J. Biela. *(Corresponding authors: Pan Sun; Yan Liang.)*

Lei Wang, Pan Sun, Yan Liang, Li He, and Xusheng Wu are with the School of Electrical Engineering, Naval University of Engineering, Wuhan 430030, China (e-mail: 19100506@nue.edu.cn; 1007101026@nue.edu.cn; 20100502@nue.edu.cn; 1610061147@nue.edu.cn; 0910061003@nue.edu.cn).

Qijun Deng is with the School of Electrical Engineering and Automation, Wuhan University, Wuhan 430072, China (e-mail: dqj@whu.edu.cn).

Color versions of one or more figures in this article are available at https://doi.org/10.1109/TPEL.2023.3326248.

Digital Object Identifier 10.1109/TPEL.2023.3326248

which increases additional hardware and software costs, and strong magnetic field interference may affect communication stability. In addition, wireless communication is not suitable for some specific applications, such as underwater and aerospace [12]. And the wireless communication module has a large time delay, which will affect the dynamic adjustment performance of the system.

To avoid the problems of the primary-side control strategy, the control strategy based on primary-side parameter identification has attracted the attention of researchers [23], [24], [25], [26], [27]. The basic principle of this kind of the control strategy is to identify the secondary-side unknown parameters by measuring primary-side signals, and then, apply the obtained identification results to the controller to realize the system output control. The merit of this kind of control strategy is that only one controller in primary side is needed to achieve the system's output control, which requires no wireless communication module and reduces the system cost and complexity. In [23], CV charging of the IPT system with LCC-P topology is realized based on the inverter phase shift (PS) control and the identified charging voltage. However, no further analysis of CC charging control is given. In [24], aiming at the IPT system with SS and SP topology, a CC and CV charging control method based on the load identification of the primary side is proposed. This control strategy relies on a complex active power measurement circuit. In [25], an indirect control strategy is proposed by controlling the primary capacitor voltage and primary coil current, and CC and CV charging control is realized. This control strategy needs to measure the phase difference of primary voltage and current, although a circuit is designed to calculate the phase difference, the implementation process is complicated. In addition, none of the methods proposed in [23], [24], and [25] analyzed the output control under the change of mutual inductance. In [26], an indirect control strategy of the secondary current is proposed, and the CC charging control is achieved. However, the mutual inductance identification of this method still depends on the wireless communication module. In [27], by using the auxiliary coil, the identification of charging voltage and charging current is realized. And according to the identification results, the CC and CV charging control is realized by the primary-side controller.

The topology of the IPT system has frequency selectivity and load-independent CV (or CC) output characteristics. Therefore, the following two topology-based control methods for CC and CV charging control are studied in [28], [29], [30], [31], and [32].

1) *Frequency switching [28]:* First, the compensation network parameters are designed to make the system has load-independent CC and CV output characteristics at different frequencies. Then, the CC and CV charging control of the system can be achieved by switching the operating frequency of the inverter.
2) *Topology switching [29], [30], [31], [32], including secondary-side topology switching [29], [30] and primary-side topology switching [31], [32]:* With this kind of method, the system should be configured with two topologies, which has CC output characteristics and CV output characteristics, respectively, and the CC and CV charging control can be realized by switching topologies. The disadvantage of this topology switching method is that, two sets of topologies and auxiliary switches need to be configured, which will increase the cost, volume, and weight of the system.

The control strategy of frequency switching and primary-side topology switching still rely on the wireless communication module to feedback the charging information. In addition, the aforementioned charging control methods based on frequency switching and topological switching are only applicable to the condition of constant coupling state.

In summary, CC and CV charging control strategies for the communication-free IPT system include secondary-side control strategy [13], [14], [15], primary-side control strategy based on parameter identification [25], [27], and secondary-side topology switching [29], [30]. Each of these control methods has its own advantages and disadvantages. Among them, the primary-side control strategy based on parameter identification can not only minimize the secondary side weight and volume, system cost, and complexity, but also be suitable for dynamic coupling conditions, which has obvious advantages. In our previous work [33], a multiparameter joint real-time identification method was proposed. Based on the identification method in [33], two primary-side control strategies for CC and CV charging are studied and proposed in this article.

The main contributions of this article are summarized and illustrated as follows.

1) A primary-side control strategy based on the identification results of charging parameters and PID controller is proposed, and its working principles is analyzed and discussed in detail.
2) A novel primary-side control strategy based on a fast calculation of conduction angle is proposed, which does not require the design and adjustment process of the controller. And the process of calculating the target conduction angle according to multiparameter identification results is analyzed in detail.

The two proposed control strategies can realize CC and CV charging control of the IPT system without communication, and both are suitable for the IPT system under dynamic coupling condition. The phase-shifting control of the primary side inverter is taken as an example in this article, but the proposed control strategies can also be extended to the IPT system with dc/dc converter on the primary side. It should be noted that, the topological and frequency applicability are determined by the parameter identification method, and the control performance depends on the accuracy and speed of parameter identification. Therefore, an accurate and fast parameter identification method is the prerequisite for the proposed control strategies to achieve accurate CC and CV charging control.

The rest of this article is organized as follows. In Section II, the operating principle of the IPT system and the PS control are introduced, and the working principle of the multiple-parameter identification based on dual equivalent impedance modulus is briefly introduced. In Section III, two control strategies based on identification results are proposed, and their working principles are analyzed in detail. In Section IV, experiments are designed

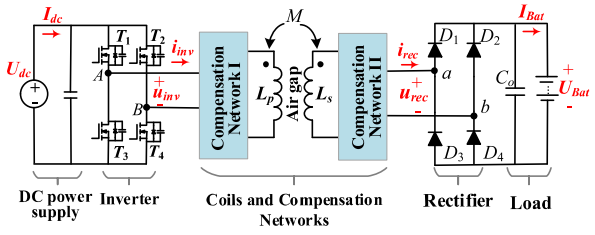

Fig. 1. IPT system structure diagram.

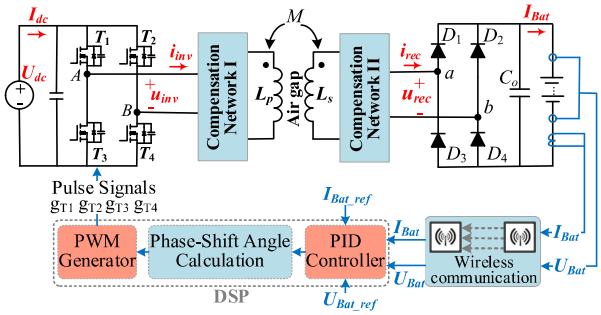

Fig. 2. PS control schematic based on wireless communication module.

to verify the feasibility of the two proposed control strategies. Finally, Section V concludes this article.

II. IPT System, PS Control, and Multiparameter Identification

A. IPT System Structure

The typical IPT system structure is shown in Fig. 1. A single-phase full-bridge inverter consisting of four MOSFETs (T_1∼T_4) is adopted to invert the dc supply voltage $U_{\rm dc}$ to a high-frequency square wave voltage $u_{\rm inv}$. A loosely coupled transformer is composed of the primary-side coil L_p and secondary-side coil L_s, where loosely means that the mutual inductance M is small, while the leakage inductances are large. To compensate these leakage inductances, various compensation network topologies with different output characteristics have been proposed [34], [35], [36]. Finally, the voltage $u_{\rm rec}$ at the receiver side, is rectified by rectifier consisting of four diodes (D_1∼D_4) and smoothed by capacitance $C_{\rm o}$ to yield the dc output voltage $U_{\rm Bat}$ to charge the battery.

B. PS Control Strategy Based on the Wireless Communication Module

Due to the particularity of wireless power transmission of the IPT system, in practical applications, a primary-side PS control strategy with wireless communication module is generally adopted, as shown in Fig. 2. The basic principle is that the voltage and current sensors are used to detect the charging information on the secondary side, and the sampled signals are fed back to the controller in the primary side through a wireless communication module. The conduction angle α is calculated by the controller based on the comparison result of the feedback signals with

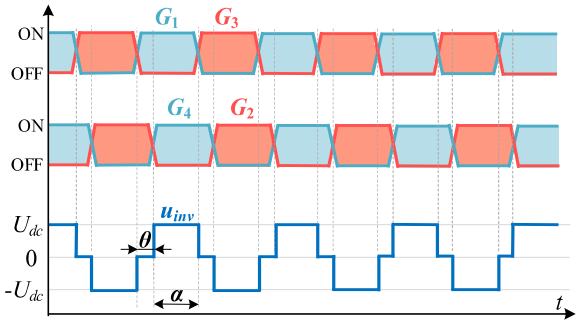

Fig. 3. Driving signals and the relationship between θ and $u_{\rm inv}$.

the reference signals. Finally, according to the conduction angle α, the corresponding drive signals are generated to control the MOSFETs' ON or OFF to change the input voltage $u_{\rm inv}$ of the IPT system. The θ is the phase-shifting angle between the leading leg (T_1 and T_3) and the lagging leg (T_2 and T_4). Since the output voltage of the inverter is generated via pulsewidth modulation (PWM), $u_{\rm inv}$ is a square wave. The waveforms of the drive signals ($g_{\rm T1}$∼$g_{\rm T4}$, corresponding to the drive signals of T_1∼T_4) and the inverter output voltage $u_{\rm inv}$ under different conduction angle α are shown in Fig. 3.

Due to the filtering effect of the compensation network, the equivalent impedance of the high-order harmonic is very large, and only the fundamental component can pass through the compensation network. Therefore, the fundamental approximation method is often adopted to analyze the circuit characteristics of the IPT system. According to the Fourier transform formula, the fundamental component of $u_{\rm inv}$ can be depicted as

$$u_{\rm inv\_}f = \frac{4U_{\rm dc}}{\pi}\sin\left(\frac{\alpha}{2}\right)\sin(\omega t) \tag{1}$$

where α is the conduction angle, and $u_{\rm inv\_}f$ is the fundamental component of $u_{\rm inv}$.

The primary-side PS control strategy relies on the wireless communication module to feedback the charging information. To reduce the system cost and complexity, the wireless communication module can be replaced by the primary-side parameter identification. In our previous work [33], we have proposed a multiparameter joint real-time identification method based on dual equivalent impedance modulus and least mean square (LMS)-based adaptive filter algorithm. The focus of this article is to study the control strategy based on parameter identification to realize CC and CV charging control of the communication-free IPT system. The parameter identification method in our previous work [33] is the basis of the control strategy proposed in this article. Therefore, the working principle of the identification method will be briefly described following.

C. Multiparameter Identification Based on Dual Equivalent Impedance Modulus

It should be noted that the proposed method and control strategy are not limited to the IPT system with a certain topology. Here, only the IPT system based on double-sided LCC (DLCC)

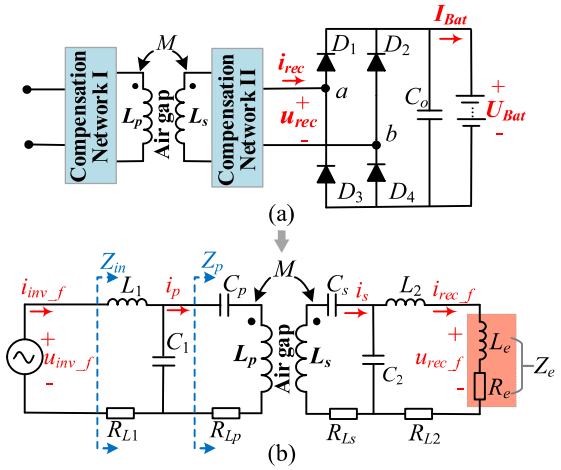

Fig. 4. Fundamental equivalent circuit of DLCC IPT system considering equivalent impedance of the rectifier.

topology is taken as an example to illustrate the operating principle of the proposed method.

The fundamental equivalent circuit of the IPT system with DLCC topology is shown in Fig. 4. The compensation network is composed of L_1, C_1, and C_p on the transmitting side and L_2, C_2, and C_s on the receiving side. L_p,L_s, and M are self-inductance of the transmit coil, self-inductance of the receive coil, and mutual inductance, respectively. R_{L1}, R_{Lp}, R_{Ls}, and R_{L2} are the stray resistances of L_1, L_p, L_s, and L_2, respectively. According to [36], the circuit parameters are designed by (2) to realize CC output independent of load, where ω_o(in rad/s) is the rated resonant frequency.

$$\omega_o = \frac{1}{\sqrt{L_1 C_1}} = \frac{1}{\sqrt{L_2 C_2}} = \frac{1}{\sqrt{(L_p - L_1)C_p}} = \frac{1}{\sqrt{(L_s - L_2)C_s}}. \tag{2}$$

According to [37], the accurate model of the rectifier load module includes two parts, which are the equivalent resistance R_e and the series equivalent inductance L_e, as shown in Fig. 4. Assuming that the equivalent load resistance of battery is $R_L = U_{\text{Bat}}/I_{\text{Bat}}$, the relationship between R_L with R_e and L_e satisfies (3).

$$\begin{cases} R_e = \dfrac{8\omega^2 L_2^2 R_L}{(\pi - 8/\pi)^2 R_L^2 + \pi^2 \omega^2 L_2^2} \\ L_e = \dfrac{8\left(1 - 8/\pi^2\right) L_2 R_L^2}{(\pi - 8/\pi)^2 R_L^2 + \pi^2 \omega^2 L_2^2} \end{cases} \tag{3}$$

where ω is the actual operating angular frequency. It should be noted that, in order to realize zero voltage switching (ZVS), the actual operating angular frequency may deviate from ω_o, which will not influence the implementation of the control strategy proposed in this article.

From Fig. 4(b), the expressions of the equivalent impedance modulus of $|Z_p|$ and $|Z_{\text{in}}|$ are established as (4) and (5), respectively, where R_L and M are the parameters to be identified.

$$|Z_p| = g_1(R_L, M) = \sqrt{X_p^2 + R_p^2} \tag{4}$$

TABLE I
ALGORITHM IMPLEMENTATION PROCESS

Algorithm

Initialization:

$R'_L(1) = 0.$

Sample data:

$I_{inv\_f\_mea}$,$U_{c1\_f\_mea}$,I_{p_mea};

Data preprocessing:

$|Z_{p\_mea}| = U_{c1\_f\_mea}/I_{p\_mea}$,

$|Z_{in\_mea}| = U_{inv\_f}/I_{inv\_f\_mea}$;

Algorithm implementation:

for n=1, 2, 3, …

$|Z_{in}(n)| = f(R'_L(n), |Z_{p\_mea}|)$;

$e(n) = |Z_{in\_mea}| - |Z_{in}(n)|$;

$\mu = g(|Z_{p\_mea}|)$;

$R'_L(n+1) = R'_L(n) + 2\mu\, e(n)|Z_{in\_mea}|$;

end

$$|Z_{\text{in}}| = g_2(R_L, M) = \sqrt{X_{\text{in}}^2 + R_{\text{in}}^2}. \tag{5}$$

By substituting the measured values of $I_{\text{inv\_}f\text{\_mea}}$, $U_{c1\_f\_\text{mea}}$, and I_{p_mea} (corresponding to the fundamental rms values of $i_{\text{inv\_}f}$, u_{c1}, and i_p, respectively) to (6) and (7), respectively, the equivalent impedance modulus of $|Z_{p\_\text{mea}}|$ and $|Z_{\text{in\_mea}}|$ can be obtained.

$$|Z_{p\_\text{mea}}| = U_{c1\_f\_\text{mea}}/I_{p\_\text{mea}} \tag{6}$$

$$|Z_{\text{in\_mea}}| = U_{\text{inv\_}f}/I_{\text{inv\_}f\text{\_mea}}. \tag{7}$$

Substitute (6) and (7) into (4) and (5), respectively, the equations about R_L and M under the dual equivalent impedance modulus constraints are established as follows

$$\begin{cases} |Z_{p\_\text{mea}}| = g_1(R_L, M) = \sqrt{X_p^2 + R_p^2} & (8.1) \\ |Z_{\text{in\_mea}}| = g_2(R_L, M) = \sqrt{X_{\text{in}}^2 + R_{\text{in}}^2} & (8.2) \end{cases}.$$

The expression of M about R_L and $|Z_{p\_\text{mea}}|$, can be obtained by transforming (8.1), as shown in (9). By substituting (9) into (8.2), the expression of $|Z_{\text{in}}|$ about R_L, and $|Z_{p\_\text{mea}}|$ can be obtained, as shown in (10). $g_1(*)$, $g_2(*)$, and $g(*)$ are function expressions.

$$M = g(R_L, |Z_{p\_\text{mea}}|) \tag{9}$$

$$|Z_{\text{in}}| = g(R_L, |Z_{p\_\text{mea}}|) = \sqrt{X_{\text{in}}^2 + R_{\text{in}}^2}. \tag{10}$$

To obtain the identification results of R_L and M from (8), which includes two complex and implicit functions, an improved LMS-based adaptive filter algorithm is adopted according to (10), and the implementation process of which is shown in Table I. In Table I, $\mu = g(|Z_{p\_\text{mea}}|)$, obtained by simulation, is the relationship between the optimal step size and the measured $|Z_{p\_\text{mea}}|$. The $\mu = g(|Z_{p\_\text{mea}}|)$ is adopted to balance the convergence speed and steady-state accuracy. According to the real-time measured values of $I_{\text{inv\_}f\text{\_mea}}$, $U_{c1\_f\_\text{mea}}$, and I_{p_mea},

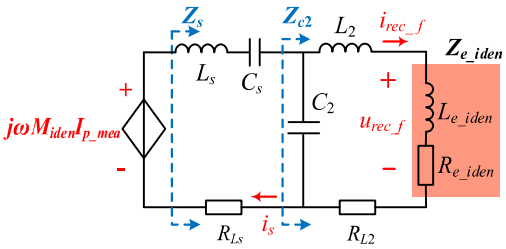

Fig. 5. Secondary side fundamental equivalent circuit.

the identification results of R_{L_iden} and M_{iden} can be obtained via the iterative calculation process shown in Table I.

Fig. 5 is the secondary-side fundamental equivalent circuit. According to Fig. 5, the I_{s_iden} (the rms value of i_s) can be obtained by substituting R_{L_iden} and M_{iden} into (11). Then, the U_{rec_f} and I_{rec_f} (the fundamental rms values of the voltage and current at the front-end of rectifier) can be obtained via substituting R_{L_iden}, M_{iden}, and I_{s_iden} into (12) as follows:

$$I_{s\_\text{iden}} = \frac{\omega M_{\text{iden}} I_{p\_\text{mea}}}{|Z_{s\_\text{iden}}|} \tag{11}$$

$$\begin{cases} I_{\text{rec}\_f} = \left| \dfrac{\frac{1}{j\omega C_2}}{\frac{1}{j\omega C_2} + j\omega L_2 + R_{L2} + Z_{e\_\text{iden}}} \right| I_{s\_\text{iden}} \\ U_{\text{rec}\_f} = |Z_{e\_\text{iden}}| \; I_{\text{rec}\_f} \end{cases}. \tag{12}$$

Finally, the identification results of battery charging voltage U_{Bat} and charging current I_{Bat} of the battery load can be obtained according to

$$\begin{cases} U_{\text{Bat\_iden}} = \frac{\pi\sqrt{2}}{4} U_{\text{rec}\_f} \\ I_{\text{Bat\_iden}} = \frac{U_{\text{Bat\_iden}}}{R_{L\_\text{iden}}} \end{cases}. \tag{13}$$

So far, the identification results of multiple parameters including M_{iden}, R_{L_iden}, R_{e_iden}, L_{e_iden}, $U_{\text{Bat\_iden}}$, and $I_{\text{Bat\_iden}}$ have been obtained. The precision and speed of the aforementioned identification method have been discussed and verified in our previous work [33], which will not be repeated here.

III. Control Strategy of Communication-Free IPT System Based on Parameter Identification

A. Analysis of the Influence of Changes in M and R_L on IPT System Output

Because the battery charging includes two stages of CC and CV charging, it is meaningful to study the output characteristics of different topologies with the change of system parameters [34], [35], [36].

We know that the DLCC IPT system has a typical advantage, that is, it has good CC output characteristic, and its resonant frequency is independent of mutual inductance and load. However, this conclusion is obtained when the rectifier is regarded as a pure resistance. In fact, accurately speaking, the rectifier load module with a capacitive filter can be equivalent to the series of a resistance (R_e) and an inductance (L_e) [37]. And the relationship between R_e, L_e, and battery equivalent resistance is shown in (3). Therefore, the output characteristics of the DLCC

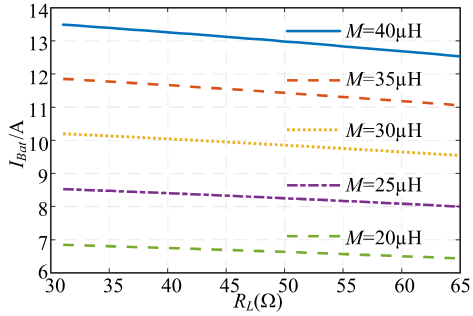

Fig. 6. I_{Bat} varies with M and R_L when $\omega = \omega_o$.

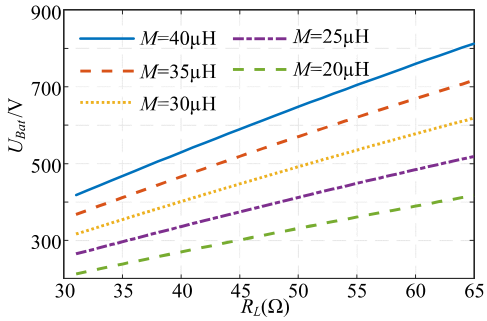

Fig. 7. U_{Bat} varies with M and R_L when $\omega = \omega_o$.

TABLE II
System's Parameters

Parameter	Value
$L_p(\mu\text{H})/R_{Lp}(\text{m}\Omega)$	146.53/530
$L_s(\mu\text{H})/R_{Ls}(\text{m}\Omega)$	146.6/510
$L_1(\mu\text{H})/R_{L1}(\text{m}\Omega)$	25.3/220
$L_2(\mu\text{H})/R_{L2}(\text{m}\Omega)$	50.24/260
$C_1(\text{nF}), C_P(\text{nF})$	138.63, 28.414
$C_2(\text{nF}), C_s(\text{nF})$	68.96, 37.67
k	0.15-0.3
$U_{Bat}(\text{V})$	300-360
$I_{Bat}(\text{A})$	10-5.54

IPT system at different M and R_L need to be rediscussed when R_e and L_e considered.

According to Fig. 4(b) and Kirchhoff's law, the relationship between U_{Bat}, I_{Bat}, M, R_e, and L_e can be given by (14) and (15), respectively. Due to the complexity of the detailed expression, it is not provided here.

$$U_{\text{Bat}} = g(M, R_L) = g(M, R_e, L_e) \tag{14}$$

$$I_{\text{Bat}} = \frac{U_{Bat}}{R_L} = g(M, R_e, L_e, R_L). \tag{15}$$

According to the (14) and (15), the corresponding U_{Bat} and I_{Bat} under different M and R_L are simulated when R_e and L_e are considered, and the simulation results are as shown in Figs. 6 and 7, respectively. The parameters of the simulation system are shown in Table II.

Fig. 6 shows that when the M remains constant and R_L changes little, the change in I_{Bat} is not significant, and it has good CC output characteristics. However, when R_L changes in

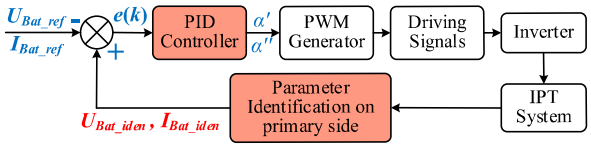

Fig. 8. Schematic diagram of the control strategy based on the PID controller and identified charging parameters.

a wide range, I_{Bat} changes significantly. To make matters worse, I_{Bat} changes greatly when M changes. Therefore, when the R_L changes greatly or M changes, the IPT system no longer has CC output characteristics. From Fig. 7, the system output voltage U_{Bat} changes significantly with M and R_L, that is, the DLCC IPT system does not have CV output characteristics.

To sum up, when there is significant fluctuation in M or R_L, the DLCC IPT system cannot maintain CC or CV output. Therefore, in different charging stages of the battery or under dynamic coupling conditions, an effective control strategy is needed to enable the system to maintain CC or CV charging.

The identification method described in Section II can identify multiple parameters in real time, including M_{iden}, R_{L_iden}, R_{e_iden}, L_{e_iden}, $U_{\mathrm{Bat\_iden}}$, and $I_{\mathrm{Bat\_iden}}$. Next, two different control strategies based on parameter identification results will be studied and discussed. One of them is a commonly adopted control strategy based on the PID controller and the identification results of battery charging information. Another is a novel proposed control strategy based on fast calculation of conduction angle. Next, the working principle of the aforementioned two control strategies will be described in detail.

B. Control Strategy Based on the PID Controller and Identification Results of Charging Information

To realize CC and CV charging control of the communication-free IPT system, the control strategy based on the PID controller and identification results of charging information is commonly adopted, and the control schematic is shown in Fig. 8. The basic working principle of this control strategy is that the PID controller adjusts the conduction angle according to the deviation between the reference signals ($U_{\mathrm{Bat\_ref}}$, $I_{\mathrm{Bat\_ref}}$) and the parameter identification results of charging information ($U_{\mathrm{Bat\_iden}}$, $I_{\mathrm{Bat\_iden}}$), so as to realize output control of the system.

Apply the multiparameter real-time identification method described in Section II to the proposed control strategy shown in Fig. 8, and the flow chart of CC and CV charging control of the communication-free IPT system based on the PID controller and identified charging information can be obtained as shown in Fig. 9.

From Fig. 9, the workflow of this control strategy can be summarized as follows. First, at the time of t_0, according to the measured $U_{c1\_f\_\mathrm{mea}}$, I_{p_mea}, $I_{\mathrm{inv\_f\_mea}}$ and the known U_{dc} and $\alpha(t_0)$, the parameter identification method described in Section II is used for parameter identification. And the identification results of $U_{\mathrm{Bat\_iden}}$ and $I_{\mathrm{Bat\_iden}}$ are obtained. Then, according to $U_{\mathrm{Bat\_iden}}$ and $I_{\mathrm{Bat\_iden}}$, it is judged whether the battery charging is in CC stage or CV stage. If the battery is in the CV charging stage,

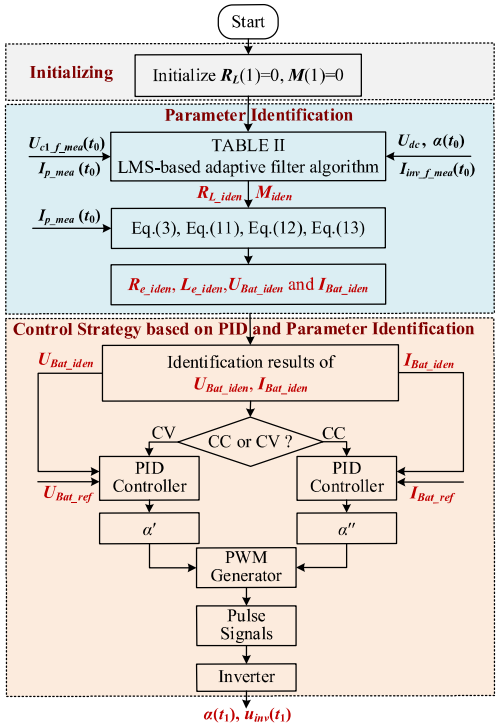

Fig. 9. Flow chart of CC and CV output control of the control strategy based on PID controller and identified charging parameters.

the PID controller adjusts the conduction angle α' according to the deviation between $U_{\mathrm{Bat\_iden}}$ and the reference voltage $U_{\mathrm{Bat\_ref}}$. If the battery is in the CC charging stage, the PID controller adjusts the conduction angle α'' according to the deviation between $I_{\mathrm{Bat\_iden}}$ and the reference current $I_{\mathrm{Bat\_ref}}$. Finally, the drive circuit generates the target conduction angle $\alpha(t_1)$ at the next moment according to the command signal α' or α''.

In fact, the essence of this kind of control strategy is that the output signals' feedback of the wireless communication module is replaced by parameter identification on the primary side.

C. Novel Control Strategy Based on Fast Calculation of the Conduction Angle

The control strategy introduced in Section III-B depends on the PID controller to calculate the conduction angle α. In this subsection, a new control strategy based on fast calculation of conduction angle is proposed. This proposed new control strategy does not require the involvement of any controller, and the target conduction angle is calculated in real time only according to the identification results of M_{iden}, R_{e_iden}, L_{e_iden}, $U_{\mathrm{Bat\_ref}}$, and $I_{\mathrm{Bat\_ref}}$. Next, the working principle and implementation process of the proposed new control strategy will be described in detail.

From Fig. 4(b), KVL equations can be derived as follows:

$$\begin{cases} (Z_{L1}+Z_{c1})\,\dot{I}_{\mathrm{inv\_}f} - Z_{c1}\,\dot{I}_p = \dot{U}_{\mathrm{inv\_}f} \\ -Z_{c1}\dot{I}_{\mathrm{inv\_}f} + (Z_{c1}+Z_{cp}+Z_{Lp})\,\dot{I}_p - Z_m\,\dot{I}_s = 0 \\ -Z_m\dot{I}_p + (Z_{Ls}+Z_{cs}+Z_{c2})\,\dot{I}_s - Z_{c2}\,\dot{I}_{\mathrm{rec\_}f} = 0 \\ -Z_{c2}\dot{I}_s + (Z_{c2}+Z_{L2}+Z_{e\_\mathrm{iden}})\,\dot{I}_{\mathrm{rec\_}f} = 0 \end{cases} \tag{16}$$

where $Z_{L1} = j\omega L_1 + R_{L1}$, $Z_{c1} = \frac{1}{j\omega C_1} + R_{c1}$, $Z_{cp} = \frac{1}{j\omega C_p} + R_{cp}$, $Z_{Lp} = j\omega L_p + R_{Lp}$, $Z_m = j\omega M_{\text{iden}}$, $Z_{Ls} = j\omega L_s + R_{Ls}$, $Z_{cs} = \frac{1}{j\omega C_s} + R_{cs}$, $Z_{c2} = \frac{1}{j\omega C_2} + R_{c2}$, $Z_{L2} = j\omega L_2 + R_{L2}$, and $Z_{e\_\text{iden}} = j\omega L_{e\_\text{iden}} + R_{e\_\text{iden}}$.

Eq. (17) can be obtained by transforming Eq. (16). In Eq. (17), $Z_4 = Z_{c2} + Z_{L2} + Z_{e\_\text{iden}}$, $Z_3 = Z_{Ls} + Z_{cs} + Z_{c2}$, $Z_2 = Z_{c1} + Z_{cp} + Z_{Lp}$, $Z_1 = Z_{L1} + Z_{c1}$.

Combining (1), (17), and (18) shown at the bottom of this page, can be obtained. Equation (18) is simplified to obtain the phasor expression of i_{rec_f}, the fundamental component of the current at the front of rectifier, as shown in (19) shown at the bottom of this page. According to (19), the rms value of i_{rec_f} can be depicted as (20) shown at the bottom of this page.

The rms value of the fundamental component of the rectifier front-end voltage satisfies the following equation, where $Z_{e\_\text{iden}} = R_{e\_\text{iden}} + j\omega L_{e\_\text{iden}}$:

$$U_{\text{rec}\_f} = |Z_{e\_\text{iden}}| \ I_{\text{rec}\_f} \tag{21}$$

$$\begin{cases} U_{\text{Bat}} = \frac{\pi\sqrt{2}}{4} U_{\text{rec}\_f} & (22.1) \\ I_{\text{Bat}} = \frac{U_{\text{Bat}}}{R_{L\_\text{iden}}} . & (22.2) \end{cases}$$

The battery charging voltage and current, U_{Bat} and I_{Bat}, can be derived as (22). The battery charging voltage U_{Bat} is assumed to be equal to the reference output voltage $U_{\text{Bat\_ref}}$, and the conduction angle to maintain the reference output voltage (CV charging stage) can be calculated accordingly. By combining (20), (21), and (22.1), $\sin\frac{\alpha'}{2}$ can be expressed by (23) shown at the bottom of this page. And then, according to (23), the α' for CV charging can be depicted as (24). The α' is the corresponding conduction angle to maintain CV output under the circumstances of M or R_L disturbance, which is temporarily called the target conduction angle.

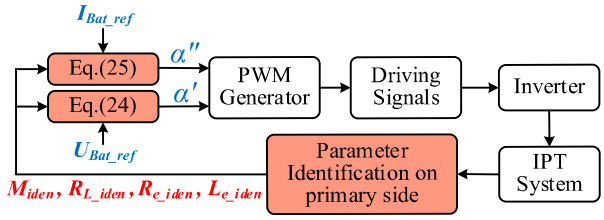

Fig. 10. Schematic diagram of the proposed control strategy based on fast calculation of the conduction angle.

$$\alpha' = 2 \cdot \arcsin\left(\frac{U_{\text{Bat\_ref}} . g\left(M_{\text{iden}}, R_{e\_\text{iden}}, L_{e\_\text{iden}}\right)}{U_{\text{dc}} \left|Z_{e\_\text{iden}}\right|}\right). \tag{24}$$

Similarly, the target conduction angle α'' to maintain the reference current under the circumstances of M or R_L disturbance can be depicted as follows:

$$\alpha'' = 2 \cdot \arcsin\left(\frac{I_{\text{Bat\_ref}} . R_{L\_\text{iden}} . g\left(M_{\text{iden}}, R_{e\_\text{iden}}, L_{e\_\text{iden}}\right)}{U_{\text{dc}} \left|Z_{e\_\text{iden}}\right|}\right). \tag{25}$$

According to the aforementioned theoretical analysis, the control schematic and flow chart for CC and CV charging of the new proposed control strategy based on fast calculation of the conduction angle are shown in Figs. 10 and 11, respectively.

From Figs. 10 and 11, the working principle and workflow of this control strategy can be summarized as follows. First, the identification results are obtained via the real-time multi-parameter identification method described in Section II. Then, similarly, according to $U_{\text{Bat\_iden}}$ and $I_{\text{Bat\_iden}}$, it is judged whether the battery charging is in the CC charging stage or CV charging stage. If the battery is in the CV charging stage, by substituting the M_{iden}, R_{e_iden}, L_{e_iden}, and $U_{\text{Bat\_ref}}$ into (24), the target

$$\begin{cases} \dot{I}_s = \frac{Z_4 \cdot \dot{I}_{\text{rec}\_f}}{Z_{c2}} \\ \dot{I}_p = \frac{Z_3 Z_4 - Z_{c2}^2}{Z_{c2} Z_m} \cdot \dot{I}_{\text{rec}\_f} \\ \dot{I}_{\text{inv}\_f} = \frac{Z_3 Z_4 Z_2 - Z_2 \cdot Z_{c2}^2 - Z_m^2 \cdot Z_4}{Z_{c1} Z_{c2} Z_m} \cdot \dot{I}_{\text{rec}\_f} \\ \dot{U}_{\text{inv}\_f} = \frac{Z_1 Z_3 Z_4 Z_2 - Z_1 Z_2 \cdot Z_{c2}^2 - Z_1 Z_m^2 \cdot Z_4 - Z_{c1}^2 Z_3 Z_4 + Z_{c1}^2 Z_{c2}^2}{Z_{c1} Z_{c2} Z_m} \cdot \dot{I}_{\text{rec}\_f} \end{cases} \tag{17}$$

$$\frac{4}{\pi} U_{\text{dc}} \sin\frac{\alpha}{2} = \frac{Z_1 Z_3 Z_4 Z_2 - Z_1 Z_2 \cdot Z_{c2}^2 - Z_1 Z_m^2 \cdot Z_4 - Z_{c1}^2 Z_3 Z_4 + Z_{c1}^2 Z_{c2}^2}{Z_{c1} Z_{c2} Z_m} \cdot \dot{I}_{\text{rec}\_f} \tag{18}$$

$$\dot{I}_{\text{rec}\_f} = \frac{Z_{c1} Z_{c2} Z_m}{Z_1 Z_3 Z_4 Z_2 - Z_1 Z_2 \cdot Z_{c2}^2 - Z_1 Z_m^2 \cdot Z_4 - Z_{c1}^2 Z_3 Z_4 + Z_{c1}^2 Z_{c2}^2} \cdot \frac{4}{\pi} U_{\text{dc}} \sin\frac{\alpha}{2} \tag{19}$$

$$I_{\text{rec}\_f} = \left| \frac{Z_{c1} Z_{c2} Z_m}{Z_1 Z_3 Z_4 Z_2 - Z_1 Z_2 \cdot Z_{c2}^2 - Z_1 Z_m^2 \cdot Z_4 - Z_{c1}^2 Z_3 Z_4 + Z_{c1}^2 Z_{c2}^2} \right| \cdot \frac{2\sqrt{2}}{\pi} U_{\text{dc}} \sin\frac{\alpha}{2}. \tag{20}$$

$$\begin{aligned} \sin\frac{\alpha'}{2} &= \frac{U_{\text{Bat\_ref}}}{U_{\text{dc}} \left|Z_{e\_\text{iden}}\right|} \left| \frac{Z_1 Z_3 Z_4 Z_2 - Z_1 Z_2 \cdot Z_{c2}^2 - Z_1 Z_m^2 \cdot Z_4 - Z_{c1}^2 Z_3 Z_4 + Z_{c1}^2 Z_{c2}^2}{Z_{c1} Z_{c2} Z_m} \right| \\ &= \frac{U_{\text{Bat\_ref}}}{U_{\text{dc}} \left|Z_{e\_\text{iden}}\right|} \cdot g\left(M_{\text{iden}}, R_{e\_\text{iden}}, L_{e\_\text{iden}}\right) . \end{aligned} \tag{23}$$

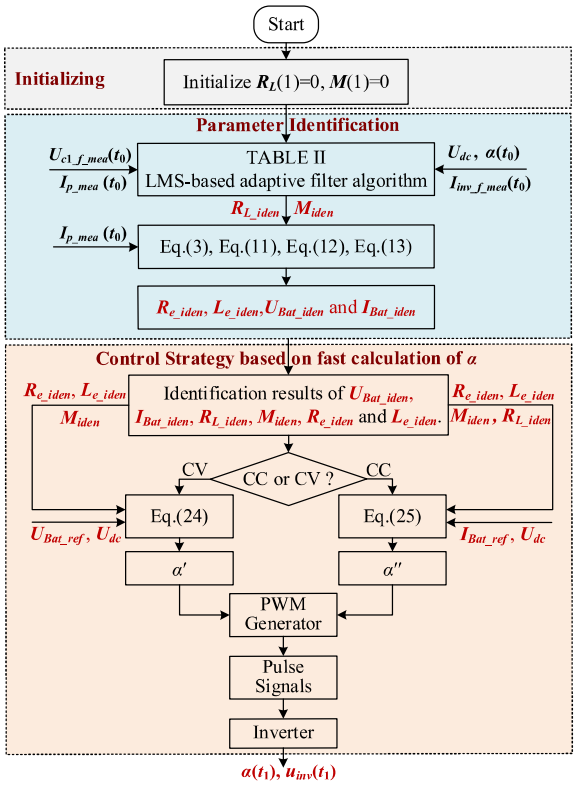

Fig. 11. Flow chart of CC and CV output control the proposed control strategy based on fast calculation of conduction angle.

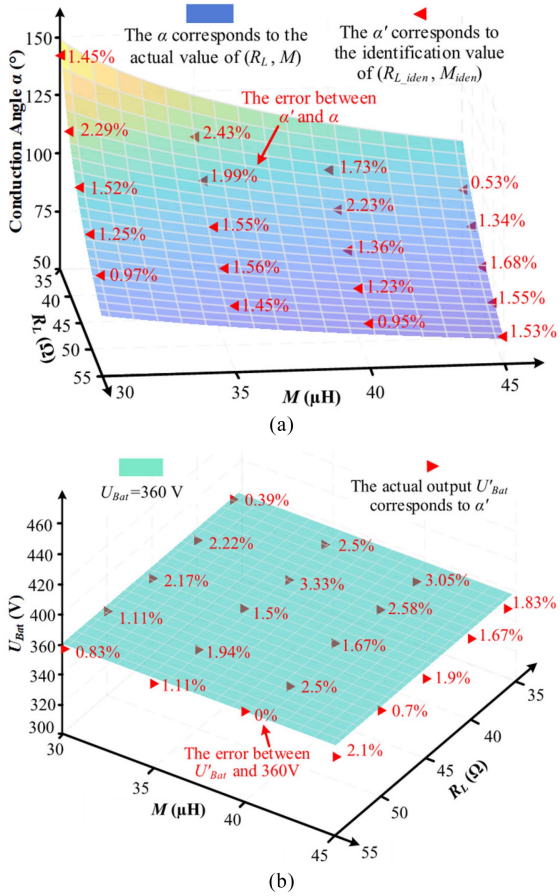

Fig. 12. Simulation comparison of CV charging with 360 V. (a) α for CV charging and the α' calculated according to the identification results. (b) Output voltage of the proposed control strategy and the reference output voltage of 360 V.

conduction angle α' for CV charging is calculated. If the battery is in the CC charging stage, target conduction angle α'' for CC charging is calculated by substituting the M_{iden}, R_{e_iden}, L_{e_iden}, R_{L_iden}, and $I_{\text{Bat\_ref}}$ into (25). Finally, the drive circuit generates the target conduction angle $\alpha(t_1)$ at the next moment according to the command signal α' or α''.

To verify the feasibility of the aforementioned theoretical analysis, simulations are carried out on the built simulation system with parameters corresponding to Table II. To ensure MOSFETs' ZVS within a large load range, an operating frequency of 80 kHz is adopted, and the dc input voltage is set to 380 V. Under different (R_L, M), the parameter identification method described in Section II is adopted to obtain the identification results, including M_{iden}, R_{e_iden}, L_{e_iden}, and R_{L_iden}. According to the identification results, the corresponding conduction angles α' under CV charging with 360 V are calculated, as shown by the red dots in Fig. 12(a). The curved surface in Fig. 12(a) is the target α to maintain the output voltage of 360 V. The red numbers in Fig. 12(a) represent the error between the calculated α' and the target α. And then, under different (R_L, M), the conduction angle of inverter is set to α' corresponding to Fig. 12(a), and the output voltages at different (R_L, M) of the simulation system are obtained as shown in Fig. 12(b). The curved surface in Fig. 12(b) represents the target output voltage of 360 V, the red dots represent the system output voltage U'_{Bat} when the proposed control strategy is adopted, and the red numbers represent the error between the aforementioned two types of voltage. Simulation results of Fig. 12 show that there are but small errors between the α' calculated by the proposed control strategy and the target α, and between the U'_{Bat} and the target voltage 360 V. And the errors mainly come from the parameter identification process.

Similarly, in the CC charging stage with 10 A, the proposed control strategy is adopted for simulation, and the simulation results are shown in Fig. 13. Fig. 13(a) shows the comparison between the target α and the α'' calculated according to identification results. And Fig. 13(b) shows the comparison between the system output current when the proposed control strategy is adopted and the target current 10 A. From Fig. 13(b), the output current with the proposed control strategy is stable near the reference current, although there is a small error between the two types of current.

So far, two control strategies based on parameter identification for CV and CC charging control of communication-free IPT system have been presented in detail. Next, the control performance of these two control strategies will be verified, compared, and analyzed by more experiments.

IV. Experimental Verification, and Discussion

A. Experimental Platform and System Parameters

In order to verify the feasibility of the aforementioned two control strategies, and to study the difference in control performance between the two control strategies, a 3.6-kW prototype

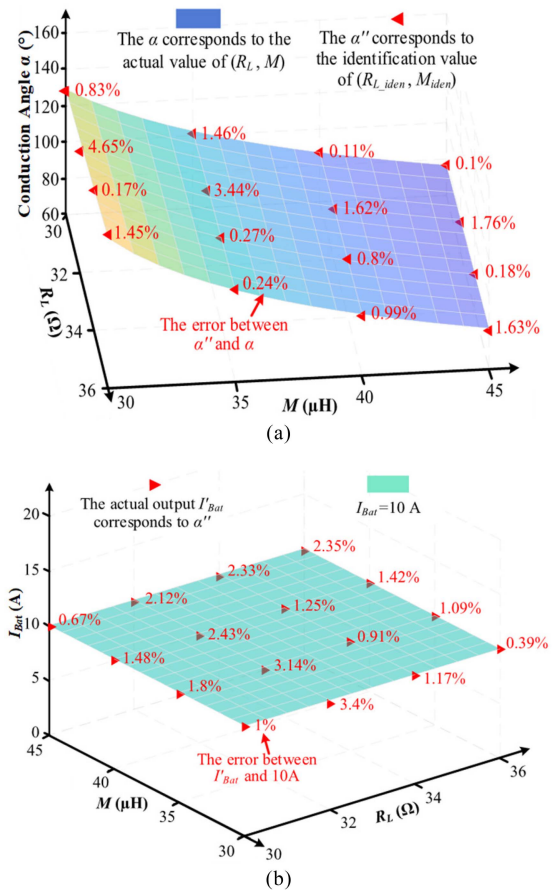

Fig. 13. Simulation comparison of CC charging with 10 A. (a) α for CC charging and the α'' calculated according to the identification results. (b) Output current of the proposed control strategy and the reference output current of 10 A.

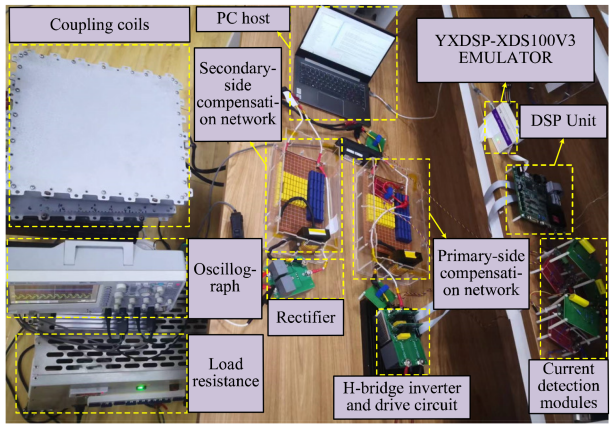

Fig. 14. Experiment platform.

platform of DLCC IPT system are developed, as shown in Fig. 14. The experimental prototype includes dc power module (REG75030), single-phase bridge inverter and drive unit, DSP control unit (TMS320F28335), primary and secondary side compensation network, transmitting and receiving coils, uncontrollable rectifier bridge module, and load resistance box.

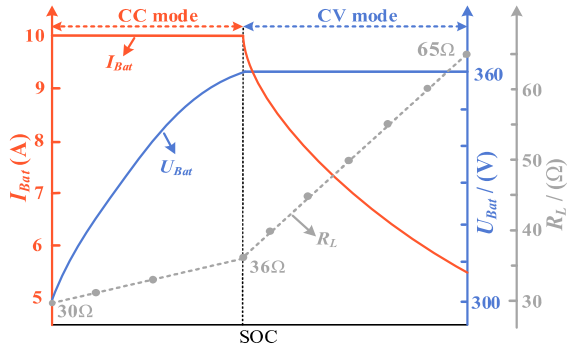

Fig. 15. Schematic diagram of two-stage charging with CC and CV.

The parameters of the compensation network elements and other components of the system are shown in Table II, and the parameters of compensation network components are accurately measured by an *LCR* Meter TH2826.

Battery charging includes two stages: CC and CV charging stage. In this platform, 10 A is taken as the target output current in the CC charging stage, and 360 V is taken as the target output voltage in the CV charging stage. The basic principle of the CC/CV two-stage charging strategy is as follows. At the initial stage, charge the battery with CC of 10 A, and the battery voltage slowly increases. When the battery voltage reaches 360 V, the output voltage is controlled to maintain 360 V for battery charging, until the battery is full. The schematic diagram of the CC and CV two-stage charging is shown in Fig. 15. During the CC charging stage, the variation range of the equivalent load resistance of the battery is 30–36 Ω. And during the CV charging stage, the variation range of R_L is 36∼65 Ω.

To verify the feasibility of the aforementioned two proposed control strategies, three types of dynamic experiments were designed. The first type of experiment is CV output control experiment with 360 V under load disturbance. The secondary type of experiment is CV output control with 360 V under mutual inductance change. And the third type of experiment is CC output control with 10 A under mutual inductance change.

The process of the experiment is as follows. First, the sampled signals ($I_{\text{inv\_}f\text{\_mea}}$, $U_{c1\_f\_\text{mea}}$, and I_{p_mea}) are substituted into the parameter identification method described in Section II (the calculation process is carried out in DSP) to obtain the real-time identification results. Then, according to the identification results, the two aforementioned control strategies are adopted to carry out the three types of experiments, respectively, and the process of the aforementioned three types of experiments will be detailed in the following subsections.

For convenience of description, the control strategy based on fast calculation of conduction angle is referred to as control strategy *A*, and the PID-based control strategy is referred to as control strategy *B* in the following discussions. In addition, to meet the output capacity of the system under different working conditions, and maintain the ZVS state of the inverter within the widest possible load range, the dc input voltage will be properly adjusted through the PC host before each type of experiment.

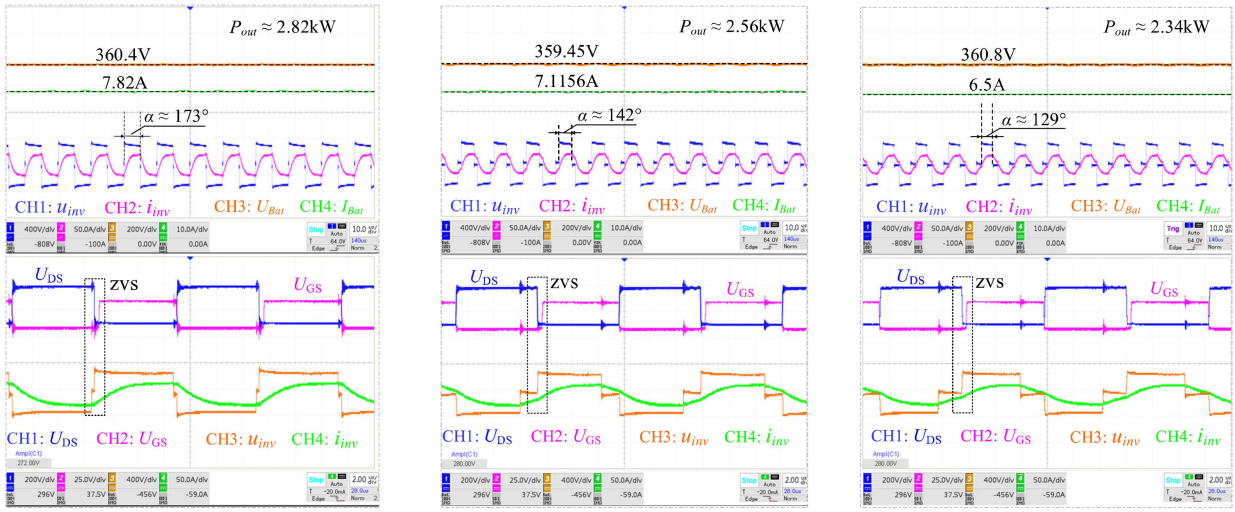

Fig. 16. When $M = 33.05$ μH, the output and conduction angle corresponding to different R_L. (a) When $R_L = 45.5$ Ω. (b) When $R_L = 50.5$ Ω. (c) When $R_L = 55.5$ Ω.

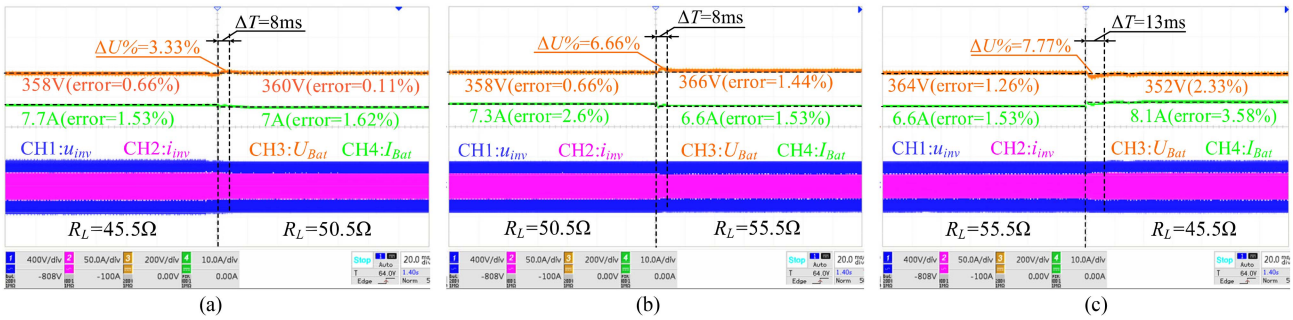

Fig. 17. Control strategy *A* is adopted, when $M = 33.05$ μH. (a) When R_L changes from 45.5 to 50.5 Ω. (b) When R_L changes from 50.5 Ω to 55.5 Ω. (c) When R_L change from 55.5 Ω to 45.5 Ω.

B. CV Charging Control Experiment When R_L Changes

The dc input voltage is set to 285 V, and the relative position between the coils is fixed at $M = 33.05$ μH. The target conduction angles corresponding to CV output with 360 V are calculated under the R_L is 45.5, 50.5, and 55.5 Ω, respectively, and the experimental waveforms of the three sets of equivalent loads are obtained, as shown in Fig. 16(a)–(c). As can be seen from Fig. 16, in all the three aforementioned cases, the inverter's ZVS can be achieved. The ZVS of the inverter can not only reduce the switching loss, but also avoid the influence of the inverter hard switching on the control performance. The subsequent experiments are carried out in inverter's ZVS, it will not be repeated description next.

In the case of R_L changes, the two control strategies based on the aforementioned parameter identification are adopted to control CV output with 360 V, and the experiments results are shown in Figs. 17–19. Fig. 17(a)–(c) are the dynamic experiments results when the control strategy *A* is adopted under different operating conditions with load disturbance. Fig. 18(a)–(c) are the dynamic experiments results when the control strategy *B* is adopted. Experimental results of Figs. 17 and 18 show that, the aforementioned two control strategies can effectively realize CV output control of the communication-free IPT system. By comparing Figs. 17 and 18, it can be found that the dynamic response speed of the control strategy *A* is faster than that of the control strategy *B*, and the overshoot is lower than that of the control strategy *B*. The control performance of the two control strategies under different load disturbance is summarized in Fig. 19. It can be seen from Fig. 19 that no matter what kind of load disturbance, the response speed of the control strategy *A* is faster than that of the control strategy *B*.

To sum up, the two proposed control strategies based on parameter identification can realize the CV charging control of the communication-free IPT system. Under the circumstances of R_L changes from 45.5 to 50.5 Ω and changes from 50.5 to 55.5 Ω, the response time of the control strategy *A* is about 8 ms, and the response time of the control strategy *B* is about 12 ms. This is completely adequate for battery charging applications, where the equivalent battery load changes slowly rather than jumps suddenly.

Although there is a small error in steady state, the error mainly comes from the measurement circuit and identification error, and it is independent of the control strategy itself. By comparing

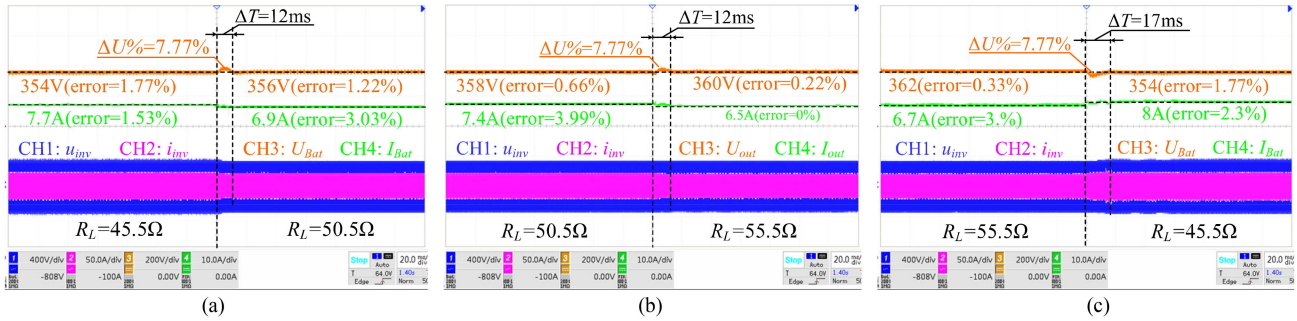

Fig. 18. Control strategy B is adopted when $M = 33.05$ μH. (a) When R_L changes from 45.5 to 50.5 Ω. (b) When R_L changes from 50.5 to 55.5 Ω. (c) When R_L changes from 55.5 to 45.5 Ω.

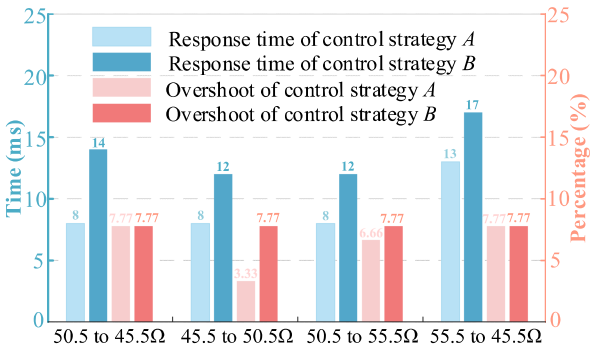

Fig. 19. Comparison of control performance between aforementioned two control strategies when maintaining CV charging with 360 V, at $M = 33.05$ μH.

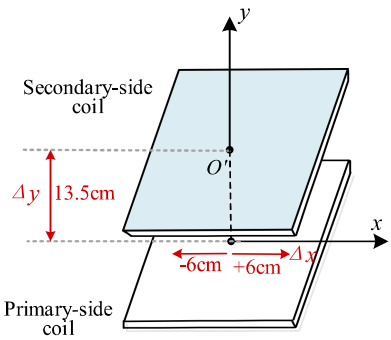

Fig. 20. Diagram of the moving direction of the secondary-side coil.

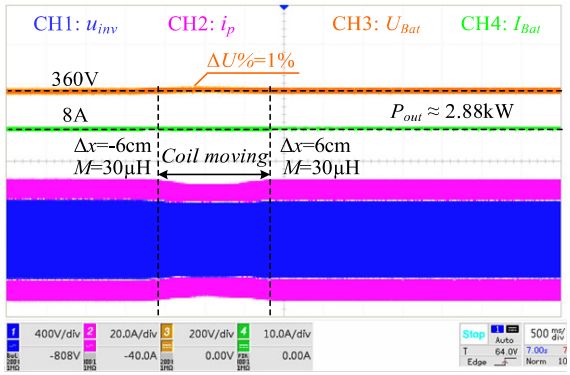

Fig. 21. Dynamic experimental results of CV output control with 360 V by control strategy A when M suddenly changes.

the dynamic experimental results of different load disturbances under the two control strategies, it is found that the control strategy A has better control performance.

C. CV Charging Control Experiment When M Changes

Two different types of experiments for mutual inductance changing are designed to verify whether the proposed control strategies can effectively achieve CV charging control under mutual inductance disturbance. The first type is the sudden change of M (fast pull the receiving coil), and the second type is the continuous change of M (continuously move the receiving coil). The following will explain the experimental process.

It should be noted that the control performance may be related to the moving speed of coil. Therefore, during the experiment, try to keep the coil moving speed consistent under different control strategies.

1) *The CV charging control with 360 V under the sudden change of M:* The dc input voltage is set to 315 V, and $R_L = 45$ Ω. When the longitudinal distance between the coils is fixed at $\Delta y = 13.5$ cm, the receiving coil is suddenly pulled to move from $\Delta x = -6$ cm ($M = 30$ μH) to $\Delta x = +6$ cm ($M = 30$ μH), and the relative position between the coils is shown in Fig. 20. The aforementioned two control strategies are used to control CV output with 360 V, and the experimental waveforms are shown in Figs. 21 and 22, respectively.

It can be seen from Figs. 21 and 22 that, in the case of sudden change of M, both control strategies can achieve CV charging control. In comparison, the maximum overshoot of control strategy A is 1%, and the maximum overshoot of the control strategy B is 6.7%. Therefore, under the condition of sudden change of M, the control strategy A has better control performance than that of the control strategy B.

2) *The CV charging control with 360 V under continuous change of M:* The dc input voltage is set to 315 V, and the R_L is fixed at 45 Ω. When the longitudinal distance

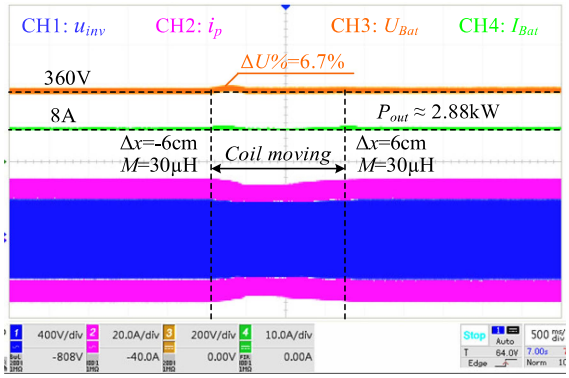

Fig. 22. Dynamic experimental results of CV output control with 360 V by control strategy *B* when M suddenly changes.

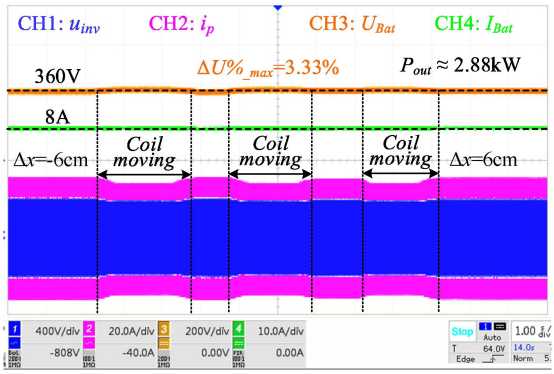

Fig. 23. Dynamic experimental results of CV output control with 360V by control strategy *A* when M changes continuously.

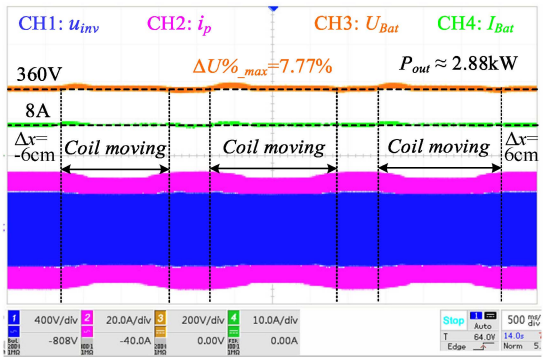

Fig. 24. Dynamic experimental results of CV output control with 360 V by control strategy *B* when M changes continuously.

between coils is fixed at $\Delta y = 13.5$ cm, the receiving coil is continuously moved back and forth between $\Delta x = -6$ cm and $\Delta x = +6$ cm in the horizontal direction, and the corresponding mutual inductance range is $M = 30 \sim 33.5\,\mu$H. Two control strategies are used to realize CV output control with 360 V, and the experimental results are shown in Figs. 23 and 24, respectively.

Comparing Figs. 23 and 24, it is obvious that although the control strategy *B* can maintain the output voltage near 360 V, the fluctuation is larger. In other words, in comparison, when the mutual inductance changes continuously, the output voltage of control strategy *A* is more stable and the overshoot is lower than those of the control strategy *B*.

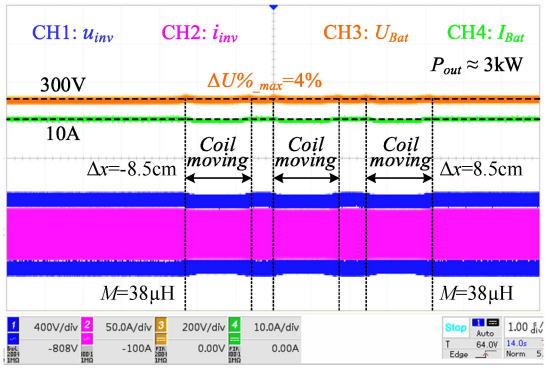

Fig. 25. Dynamic experimental results of CC output control with 10 A by control strategy *A* when M changes continuously.

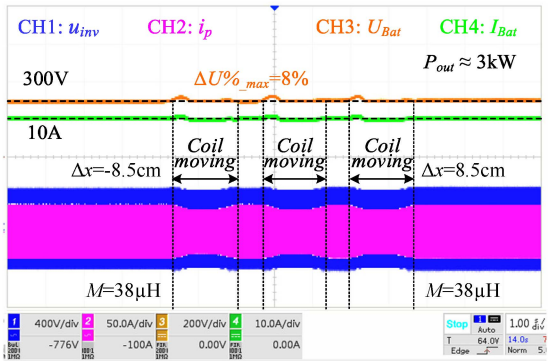

Fig. 26. Dynamic experimental results of CC output control with 10 A by control strategy *B* when M changes continuously.

D. CC Charging Control Experiment When M Changes

A set of experiments with continuous changes of mutual inductance are designed to verify whether the proposed control strategy can effectively realize CC charging control under continuous change of M. The dc input voltage is set to 350 V, and the R_L is fixed at 30 Ω. When the longitudinal distance between coils is fixed at $\Delta y = 12.4$ cm, the receiving coil is continuously moved back and forth between $\Delta x = -8.5$ cm and $\Delta x = +8.5$ cm in the horizontal direction, and the corresponding mutual inductance range is $M = 30 \sim 38\ \mu$H. Two control strategies are used to realize CC output control with 10 A, and the experimental results are shown in Figs. 25 and 26, respectively.

Comparing Figs. 25 and 26, it can be found that under the circumstances of continuous change of M, the maximum voltage fluctuation of control strategy *A* is 4%, and that of the control strategy *B* is 8%. In other words, when the mutual inductance changes continuously, the output voltage and current of the control strategy *A* is more stable and the fluctuation is smaller than those of the control strategy *B*.

The aforementioned series of dynamic experimental results show that the proposed two control strategies based on parameter identification can realize the CC and CV charging control of the communication-free IPT system with a small error in steady

TABLE III
COMPARISON TO THE EXISTING PRIMARY-SIDE CONTROL STRATEGIES BASED ON PARAMETER IDENTIFICATION

Features	Number of controllers	Communication -free	CC and CV	Suitable for dynamic M	Power	Load	Response time	Oversh oot	Static error
[23]	1	Yes	Only CV	No	150 W	-	-	-	-
[24]-[25]	1	Yes	CC and CV	No	<150 W	20.15 → 58.63Ω	-	-	0%
[26]	1	No	Only CC	No	430~580 W	-	-	-	-
[27]	1	Yes	CC and CV	Yes	202 W	-	-	-	-
Control strategy A of this article	No need	Yes	CC and CV	Yes	2.34~2.82 kW	45.5→ 55.5Ω	8~13ms	3.33% ~ 7.77%	0%~ 2.33%
Control strategy B of this article	1	Yes	CC and CV	Yes	2.34~2.82 kW	45.5→ 55.5Ω	12~17ms	7.77%	0%~ 1.77%

state. The error mainly comes from the identification error of parameter identification. In fact, the dynamic response time is also directly related to the identification rate. Therefore, accurate and fast parameter identification method is the key to achieve effectively CC and CV charging control based on parameter identification.

There have been some research achievements in charging control of the IPT system based on parameter identification, and these control methods have their own characteristics, as shown in Table III, in which the last four columns are the dynamic regulation performance for CV charging control when R_L changes. Among these control strategies, only the control strategy A proposed in this article can realize the CC and CV charging control, under the condition of M disturbance and R_L disturbance without the design and adjustment of any controller. Only the two control strategies proposed in this article have discussed the dynamic adjustment effect under M disturbance and R_L disturbance in detail, and the response time is significantly lower than the control strategy based on the wireless communication module (tens of millisecond) [38], [39], [40].

In addition, it can be seen from Table III that, the dynamic response time of the control strategy A is shorter than that of the control strategy B. This is because the control strategy A does not depend on the adjustment of the controller, but directly calculates the value of the conduction angle according to the identification results, which saves the adjustment time of the controller to a certain extent.

Although the two proposed control strategies based on parameter identification do not require wireless communication modules and have a short response time, their steady-state accuracy is limited by the parameter identification accuracy, and there will be inevitable static errors, as shown in Table III. Therefore, to further improve the control performance of the control strategy based on parameter identification, it is an effective means to propose a faster and more accurate parameter identification method with low sensitivity to compensation network parameters. This is also our next focus and research direction. In addition, consistent with the applicable scope of the parameter identification method in [33], the two proposed control strategies in this article are also limited to CCM operating condition of the rectifier.

V. CONCLUSION

Based on our previous work, two control strategies based on parameter identification are proposed in this article to achieve CC and CV charging control of the communication-free IPT system. One of them is the control strategy based on the PID controller and identified battery charging parameters, and another is the control strategy based on fast calculation of conduction angle. The working principles of the two control strategies for CC and CV charging are described in detail. Dynamic experiments under different parameter disturbance are designed to verify the feasibility of the two control strategies. Therefore, the research work done in this article is that, the control strategy based on parameter identification have been explored, which provides a research basis for the engineering realization of closed-loop control of the communication-free IPT system in the future.

The following conclusions can be drawn from the theoretical and experimental results.

1) The experimental results show that both the two control strategies based on parameter identification can realize the CC and CV charging control of the communication-free IPT system. And the response time of the two proposed control strategies is shorter than that of the control strategy based on wireless communication.
2) The control strategy based on fast calculation of conduction angle does not depend on a certain controller to adjust the conduction angle. It omits the complicated design process of controller, and saves the time for the controller to dynamically adjust the conduction angle. Therefore, the experimental results show that, the dynamic performance of the control strategy based on fast calculation of conduction angle is better than that of the control strategy based on the PID controller and identified battery charging parameters.
3) The steady-state accuracy of the control strategy based on parameter identification is limited by the identification accuracy. Therefore, how to optimize the parameter identification method to improve the control performance of the control strategy based on parameter identification is worthy of further study.

REFERENCES

[1] S. C. Tang, T. L. T. Lun, Z. Guo, K.-W. Kwok, and N. J. McDannold, "Intermediate range wireless power transfer with segmented coil transmitters for implantable heart pumps," *IEEE Trans. Power Electron.*, vol. 32, no. 5, pp. 3844–3857, May 2017.

[2] S. C. Tang, "A low-operating-voltage wireless intermediate-range scheme for energy and signal transmission by magnetic coupling for implantable devices," *IEEE J. Emerg. Sel. Topics Power Electron.*, vol. 3, no. 1, pp. 242–251, Mar. 2015.

[3] G. B. Joun and B. H. Cho, "An energy transmission system for an artificial heart using leakage inductance compensation of transcutaneous transformer," *IEEE Trans. Power Electron.*, vol. 13, no. 6, pp. 1013–1022, Nov. 1998.

[4] S. Y. R. Hui, "Planar inductive battery charging system," U.S. Patent 7576514, Aug. 18, 2009.

[5] S. Y. R. Hui and W. C. Ho, "A new generation of universal contactless battery charging platform for portable consumer electronic equipment," *IEEE Trans. Power Electron.*, vol. 20, no. 3, pp. 620–627, May 2005.

[6] X. Liu and S. Y. Hui, "Simulation study and experimental verification of a contactless battery charging platform with localized charging features," *IEEE Trans. Power Electron.*, vol. 22, no. 6, pp. 2202–2210, Nov. 2007.

[7] J. Huh, S. W. Lee, W. Y. Lee, G. H. Cho, and C. T. Rim, "Narrow-width inductive power transfer system for online electrical vehicles," *IEEE Trans. Power Electron.*, vol. 26, no. 12, pp. 3666–3679, Dec. 2011.

[8] G. A. Covic, J. T. Boys, M. L. G. Kissin, and H. G. Lu, "A three-phase inductive power transfer system for roadway-powered vehicles," *IEEE Trans. Ind. Electron.*, vol. 54, no. 6, pp. 3370–3378, Dec. 2007.

[9] J. Sallán, J. L. Villa, A. Llombart, and J. F. Sanz, "Optimal design of ICPT systems applied to electric vehicle battery charge," *IEEE Trans. Ind. Electron.*, vol. 56, no. 6, pp. 2140–2149, Jun. 2009.

[10] Y. Chen, S. He, B. Yang, S. Chen, Z. He, and R. Mai, "Reconfigurable rectifier-based detuned series-series compensated IPT system for anti-misalignment and efficiency improvement," *IEEE Trans. Power Electron.*, vol. 38, no. 2, pp. 2720–2729, Feb. 2023, doi: 10.1109/TPEL.2022.3204592.

[11] Y. Chen et al., "A clamp circuit-based inductive power transfer system with reconfigurable rectifier tolerating extensive coupling variations," *IEEE Trans. Power Electron.*, to be published, doi: 10.1109/TPEL.2023.3303487.

[12] Z. Li, H. Liu, Y. Tian, and Y. Liu, "Constant current/voltage charging for primary-side controlled wireless charging system without using dual-side communication," *IEEE Trans. Power Electron.*, vol. 36, no. 12, pp. 13562–13577, Dec. 2021, doi: 10.1109/TPEL.2021.3088272.

[13] K. Colak, E. Asa, M. Bojarski, D. Czarkowski, and O. C. Onar, "A novel phase-shift control of semi-bridgeless active rectifier for wireless power transfer," *IEEE Trans. Power Electron.*, vol. 30, no. 11, pp. 6288–6297, Nov. 2015.

[14] Y. Yang, W. Zhong, S. Kiratipongvoot, S.-C. Tan, and S. Y. R. Hui, "Dynamic improvement of series–series compensated wireless power transfer systems using discrete sliding mode control," *IEEE Trans. Power Electron.*, vol. 33, no. 7, pp. 6351–6360, Jul. 2018.

[15] S. Ann and B. K. Lee, "Analysis of impedance tuning control and synchronous switching technique for a semi-bridgeless active rectifier in inductive power transfer systems for electric vehicles," *IEEE Trans. Power Electron.*, vol. 36, no. 8, pp. 8786–8798, Aug. 2021.

[16] C. Cai, S. Wu, L. Jiang, Z. Zhang, and S. Yang, "A 500-W wireless charging system with lightweight pick-up for unmanned aerial vehicles," *IEEE Trans. Power Electron.*, vol. 35, no. 8, pp. 7721–7724, Aug. 2020.

[17] W. Wang, C. Xu, C. Zhang, and J. Yang, "Optimization of transmitting coils based on uniform magnetic field for unmanned aerial vehicle wireless charging system," *IEEE Trans. Magn.*, vol. 57, no. 6, Jun. 2021, Art. no. 8600105.

[18] U. D. Kavimandan, S. M. Mahajan, and C. W. Van Neste, "Analysis and demonstration of a dynamic ZVS angle control using a tuning capacitor in a wireless power transfer system," *IEEE J. Emerg. Sel. Topics Power Electron.*, vol. 9, no. 2, pp. 1876–1890, Apr. 2021.

[19] J. M. Miller, O. C. Onar, and M. Chinthavali, "Primary-side power flow control of wireless power transfer for electric vehicle charging," *IEEE J. Emerg. Sel. Topics Power Electron.*, vol. 3, no. 1, pp. 147–162, Mar. 2015.

[20] E. Gati, G. Kampitsis, and S. Manias, "Variable frequency controller for inductive power transfer in dynamic conditions," *IEEE Trans. Power Electron.*, vol. 32, no. 2, pp. 1684–1696, Feb. 2017.

[21] T. Diekhans and R. W. De Doncker, "A dual-side controlled inductive power transfer system optimized for large coupling factor variations and partial load," *IEEE Trans. Power Electron.*, vol. 30, no. 11, pp. 6320–6328, Nov. 2015.

[22] C. Xia, W. Wang, G. Chen, X. Wu, S. Zhou, and Y. Sun, "Robust control for the relay ICPT system under external disturbance and parametric uncertainty," *IEEE Trans. Control Syst. Technol.*, vol. 25, no. 6, pp. 2168–2175, Nov. 2017, doi: 10.1109/TCST.2016.2634502.

[23] U. K. Madawala and D. J. Thrimawithana, "New technique for inductive power transfer using a single controller," *IET Power Electron.*, vol. 5, no. 2, pp. 248–256, Feb. 2012.

[24] K. Song, Z. Li, J. Jiang, and C. Zhu, "Constant current/voltage charging operation for series-series, and series-parallel compensated wireless power transfer systems employing primary-side controller," *IEEE Trans. Power Electron.*, vol. 33, no. 9, pp. 8065–8080, Sep. 2018.

[25] Z. Li, G. Wei, S. Dong, K. Song, and C. Zhu, "Constant current/voltage charging for the inductor-capacitor-inductor-series compensated wireless power transfer systems using primary-side electrical information," *IET Power Electron.*, vol. 11, no. 14, pp. 2302–2310, Oct. 2018.

[26] Y. Wei and F. Wu, "Indirect control strategy of secondary current for LCC-series compensated wireless power transfer system based on primary current closed-loop control," *IEEE Trans. Transp. Electrific.*, vol. 8, no. 2, pp. 1553–1565, Jun. 2022, doi: 10.1109/TTE.2021.3129508.

[27] Z. Li, H. Liu, Y. Tian, and Y. Liu, "Constant current/voltage charging for primary-side controlled wireless charging system without using dual-side communication," *IEEE Trans. Power Electron.*, vol. 36, no. 12, pp. 13562–13577, Dec. 2021, doi: 10.1109/TPEL.2021.3088272.

[28] J. Lu, G. Zhu, D. Lin, S.-C. Wong, and J. Jiang, "Load-independent voltage and current transfer characteristics of the high-order resonant network in IPT system," *IEEE J. Emerg. Sel. Topics Power Electron.*, vol. 7, no. 1, pp. 422–436, Mar. 2019.

[29] Y. Li et al., "A new coil structure and its optimization design with constant output voltage and constant output current for electric vehicle dynamic wireless charging," *IEEE Trans. Ind. Electron.*, vol. 15, no. 9, pp. 5244–5256, Sep. 2019.

[30] Y. Chen, B. Yang, Z. Kou, Z. He, G. Cao, and R. Mai, "Hybrid and reconfigurable IPT systems with high-misalignment tolerance for constant-current and constant-voltage battery charging," *IEEE Trans. Power Electron.*, vol. 33, no. 10, pp. 8259–8269, Oct. 2018.

[31] X. Li, L. Yang, Z. Xu, Y. Wu, S. Liu, and C. Cai, "A communication-free WPT system based on transmitter-side hybrid topology switching for battery charging applications," *AIP Adv.*, vol. 10, 2020, Art. no. 045302.

[32] J. Wang et al., "Communication-free long-distance wireless charging system for battery load with adaptive switching of constant voltage and constant current," *IEEE Trans . Transp. Electrific.*, to be published, doi: 10.1109/TTE.2023.3294513.

[33] L. Wang et al., "Joint real-time identification for mutual inductance and load charging parameters of IPT system," *IEEE J. Emerg. Sel. Topics Power Electron.*, vol. 11, no. 4, pp. 4574–4590, Aug. 2023, doi: 10.1109/JESTPE.2023.3275138.

[34] A. Khaligh and S. Dusmez, "Comprehensive topological analysis of conductive and inductive charging solutions for plug-in electric vehicles," *IEEE Trans. Veh. Technol.*, vol. 61, no. 8, pp. 3475–3489, Oct. 2012, doi: 10.1109/TVT.2012.2213104.

[35] Y. H. Sohn, B. H. Choi, E. S. Lee, G. C. Lim, G.-H. Cho, and C. T. Rim, "General unified analyses of two-capacitor inductive power transfer systems: Equivalence of current-source SS and SP compensations," *IEEE Trans. Power Electron.*, vol. 30, no. 11, pp. 6030–6045, Nov. 2015, doi: 10.1109/TPEL.2015.2409734.

[36] S. Li, W. Li, J. Deng, T. D. Nguyen, and C. C. Mi, "A double-sided LCC compensation network and its tuning method for wireless power transfer," *IEEE Trans. Veh. Technol.*, vol. 64, no. 6, pp. 2261–2273, Jun. 2015.

[37] Y. Guo, Y. Zhang, S. Li, C. Tao, and L. Wang, "Load parameter joint identification of wireless power transfer system based on the DC input current and phase-shift angle," *IEEE Trans. Power Electron.*, vol. 35, no. 10, pp. 10542–10553, Oct. 2020, doi: 10.1109/TPEL.2020.2981651.

[38] C. Xia, W. Wang, G. Chen, X. Wu, S. Zhou, and Y. Sun, "Robust control for the relay ICPT system under external disturbance and parametric uncertainty," *IEEE Trans. Control Syst. Technol.*, vol. 25, no. 6, pp. 2168–2175, Nov. 2017, doi: 10.1109/TCST.2016.2634502.

[39] X. Wang, J. Xu, M. Leng, H. Ma, and S. He, "A hybrid control strategy of LCC-S compensated WPT system for wide output voltage and ZVS range with minimized reactive current," *IEEE Trans. Ind. Electron.*, vol. 68, no. 9, pp. 7908–7920, Sep. 2021, doi: 10.1109/TIE.2020.3013788.

[40] K. Zhang, P. Zhang, H. Du, Z. Yan, B. Song, and A. P. Hu, "Robust control of IPT system for constant current charging under multiple parameter perturbations," *IEEE Trans. Ind. Appl.*, vol. 58, no. 1, pp. 1168–1178, Jan. Feb. 2022, doi: 10.1109/TIA.2021.3097314.

Lei Wang received the M.S. degree in instrument science and technology from Southwest Petroleum University, Chengdu, China, in 2016. She is currently working toward the Ph.D. degree in electrical engineering with the Naval University of Engineering, Wuhan, China.

Her current research interests include circuit topology, analysis, and parameter identification of wireless power transfer.

Pan Sun was born in Zibo, China, in 1986. He received the B.S., M.S., and Ph.D. degrees in electrical engineering from the College of Electrical Engineering, Naval University of Engineering, Wuhan, China, in 2009, 2015, and 2022, respectively.

In June 2015, he joined the College of Electrical Engineering, Naval University of Engineering, as an Associate Research Fellow. He has authored and coauthored more than 70 papers, among which more than 30 have been published by SCI and engineering index (EI) journals such as IEEE transactions and other journals. His research interests include wireless power transfer, design of new transformer, and special motor and its control.

Dr. Sun has successively presided over the National Key Research and Development Program, the National Natural Science Foundation, and other topics. He was the recipient of five provincial and ministerial science and Technology progress awards and teaching achievement awards.

Yan Liang received the B.S. and M.S. degrees in electrical engineering and automation from the Beijing Jiaotong University of Beijing, China, in 2014 and 2017, respectively. He is currently working toward the Ph.D. degree in electrical engineering with the Naval University of Engineering, Wuhan, China.

His current research interests include robust control method and wireless power transfer.

Li He received the M.S. degree in electrical engineering, in 2022, from the Naval University of Engineering, Wuhan, China, where he is currently working toward the Ph.D. degree in electrical engineering.

His current research interests include parameter identification and control of wireless power transfer.

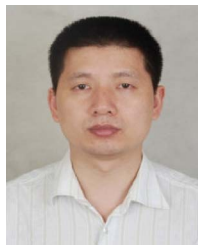

Xusheng Wu received the B.S., M.S. Tech., and Ph.D. degrees in electrical engineering from the College of Electrical and Informational Engineering, Naval University of Engineering, Wuhan, China, in 1996, 1999, and 2004, respectively.

He is currently a Professor with the College of Electrical and Informational Engineering, Naval University of Engineering. His research interests include wireless power transfer, electric devices, and power systems on warships.

Qijun Deng received the B.S. and M.Sc. degrees in mechanical engineering and the Ph.D. degree in computer application technology from Wuhan University, Wuhan, China, in 1999, 2002, and 2005, respectively.

In June 2005, he joined the Department of Automation (which now is merged into School of Electrical Engineering and Automation), Wuhan University, where he is currently a Professor. From 2013 to 2014, he was a Visiting Scholar with New York University Tandon School of Engineering, Brooklyn, NY, USA. His research interests include wireless power transfer, distribution automation, and electrical power informatic.